

Phase Equilibria in the Al-Co-Ni Alloy System

Yang Zhou¹ · Philip Nash¹ · Samuel M. Bessa¹ · Guilherme Teodoro Ferrigatto¹ ·
Bruna Santos V. P. Madureira¹ · Aparecida Silva Magalhães¹ · Aline Oliveira¹ ·
Guilherme Carvalho Pereira¹ · Lorena Goncalves Ribeiro¹ · Lucas Pires dos Santos¹ ·
André Alves da Silva¹ · Jessica Dornelas Silva¹ · Andre Gonzalez Silva¹ ·
Jean Muniz de Souza¹ · Yuri Santorio Torres¹ · Raul Lima da Silva¹ ·
Barbara Fernanda Rievers Fernandes de Cunha¹

Submitted: 16 May 2017 / in revised form: 21 July 2017 / Published online: 14 August 2017
© ASM International 2017

Abstract The phase equilibria in the Ni-Co rich region (<50 at.%Al) of the Al-Co-Ni system were studied experimentally for two isothermal sections at 1100 and 800 °C. Metallography, energy dispersive spectroscopy, hardness and x-ray diffraction were used for characterization and determination of γ , γ' and β phases within the ternary system. Phase boundaries in the isothermal sections and a partial liquidus projection are modified compared to previously published work. Comparison is made to the isothermal sections computed using Thermo-Calc and the TCNI8 database. No definitive experimental evidence corroborating the predicted existence of a Nishizawa horn was obtained.

Keywords Al-Co-Ni system · lattice parameter · phase diagram

1 Introduction

The Al-Co-Ni system is of interest as the basis for high temperature structural materials,^[1] for shape memory properties,^[2–4] catalysts^[5] and for production of large scale nanostructures.^[6] The Al-Co-Ni ternary alloy system has

been studied over many decades, with the aim of understanding the phase constitution in the system.^[7] Previous studies show that there are four phases existing in the Al-deficient region of the system: γ ((Ni): A1), γ' (Ni₃Al: L1₂), β ((Ni,Co)Al: B2) and β' (martensite (L1₀)).^[1] The crystal structures of these phases are shown in Fig. 1. The precipitation of γ' from the γ matrix makes it the basis for structural high-temperature alloys. Over a limited composition range, β phase alloys undergo a thermoelastic martensitic transformation from the B2 structure to β' (martensite with an L1₀ structure) and this transformation exhibits the shape memory effect.^[8–10] The addition of Co to Ni decreases the stacking fault energy and significantly improves the creep resistance at elevated temperature and the coarsening rate of the γ' phase.^[11]

According to the review of Ref 7 and previous reports, the isothermal sections and liquidus projection in the Al-poor region have been studied and established by Ref 8 (experimental), 12 (calculation), 13, 9 (critical review), 14 (critical review) and 1 (experimental). Ref 15 also investigated the phase relations and thermodynamic properties of Al-Co-Ni using first-principles calculations based on density functional theory (DFT) and compared their results with published experimental data from 900 to 1300 °C. There are also some phase composition data determined using electron probe microanalysis on the $\gamma + \gamma'$ phase field at 800, 750 and 700 °C.^[16] Tie-lines between γ and γ' phases were also determined by Ref 17.

Despite these studies uncertainties exist regarding the exact positions of the phase boundaries and in addition, Thermo-Calc (Database: TCNI8) isothermal sections at temperatures below 1000 °C show discrepancies with the experimental data. In particular the Thermo-Calc

Electronic supplementary material The online version of this article (doi:10.1007/s11669-017-0586-z) contains supplementary material, which is available to authorized users.

✉ Yang Zhou
yzhou76@hawk.iit.edu

✉ Philip Nash
nash@iit.edu

¹ Thermal Processing Technology Center, Illinois Institute of Technology, Chicago, IL 60616, USA

¹ (Ni) is used to represent Ni solid solution.

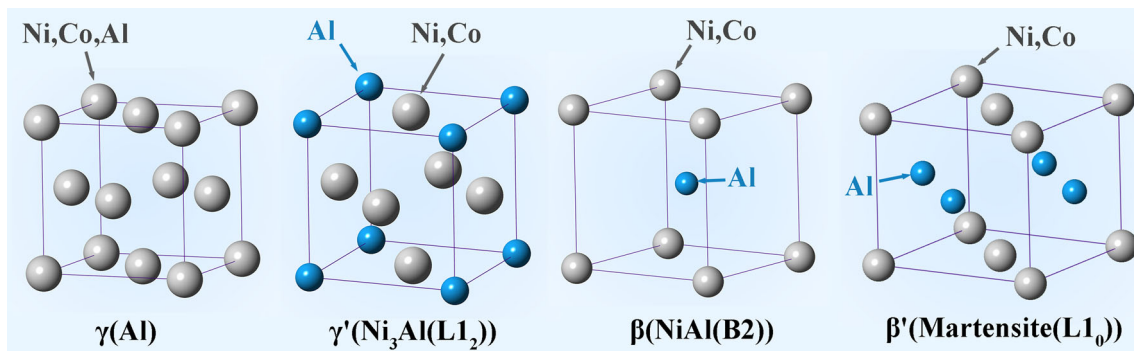


Fig. 1 Phases in the Al-Co-Ni alloy system below 50 at.%Al

calculations predict the formation of a Nishizawa horn leading to a two-phase field of ferromagnetic γ_f + paramagnetic γ_p , which has never been experimentally observed. The *Nishizawa* horn, was first reported in Ref 18 in a paper discussing the thermodynamic analysis of solubility and miscibility gaps in ferromagnetic α -Fe alloys. He found that the miscibility gap and its spinodal in α -Fe-X solid solutions are of abnormal shape, having a sharp horn or a broad bump at the Curie temperature. People later named this phenomenon the *Nishizawa* horn in his honor for describing the magnetic contributions to the Gibbs energy that lead to a two-phase field having the shape of a horn.^[19] Interestingly, such a *Nishizawa* horn was predicted using the CALPHAD approach for several Co-based binary systems long before the experimental confirmation, which is difficult to establish due to kinetic constraints.^[20,21] Recently, Ref 22 and 23 both reported calculated *Nishizawa* horns in bcc Fe-Cr and Al-Co with a first-principles based thermodynamic model and the CALPHAD method, respectively.

Therefore, more work is needed for experimental confirmation of the *Nishizawa* horn and verification of the phase boundaries in the Al-Co-Ni ternary alloy system. We have revisited the phase equilibria among the γ , γ' and β phases in the Al-Co-Ni system on the basis of previous work, modifying the isothermal sections at two temperatures—1100 and 800 °C as well as confirming the liquidus projection in the Ni-Co rich region.

2 Experimental Methods

A series of 18 Al-Co-Ni alloy samples were prepared in the composition range Ni-(10-70)at.%Co-(4-30)at.%Al as shown in Fig. 2, henceforth designated as Ni X-Y, which means X at.% of Co and Y at.% of Al. The nominal compositions of the samples are listed in Table 1. All samples were arc-melted from elemental starting materials of 99.99 wt.% purity into ingots weighing from 25 to 30 g

followed by 24 h homogenization at 1200 °C. The arc-melted ingots were weighed and the mass loss in all cases was less than 3%. The ingots from Alloys 1 to 13 were then cold rolled from 5 to 50% reduction, depending on their ductility, to assist in breaking down the cast structure and removing chemical segregation resulting from casting during subsequent annealing. The remaining alloys could not be cold rolled due to the high content of Al, making the samples brittle.

Samples 1 through 14 were then annealed at 1100 °C from 24 to 96 h, as listed in Table 1. Sample 15-18 were annealed at 1200 °C for 24 h. Subsequently all samples were annealed at 800 °C for 2 weeks and 600 °C for 4 weeks. All the annealing treatments were performed under argon atmosphere. An additional heat treatment of 240 h at 800 °C was also performed on selected samples to verify that equilibrium was achieved for the initial 2-week heat treatment.

The materials were then examined optically, after using Marble's etchant, to investigate the phase morphology existing after each annealing process. Back Scattered electron Composition mode imaging (BSC) and Energy Dispersive Spectroscopy (EDS) on a Scanning Electron Microscope (SEM) were used to observe and measure the phase composition of each sample using an accelerating voltage of 20 kV. Regions for phase analysis were carefully selected to minimize errors from adjacent phases. For each sample, 4 areas of interest were selected for phase composition analysis, where the result is an average value of 16 to 20 analyses for each phase. The hardness was evaluated using a diamond indenter with a loading of 0.3 kgf for 15 s holding time in a Micro-Vickers hardness tester. The hardness values are the average of 10 measurements. Differential scanning calorimetry (DSC) analysis was used to determine the solidus temperature of alloy samples as well as verifying the monovariant liquidus line in Al-Co-Ni. The DSC experiments were performed in a Setaram SETSYS 16/18 calorimeter under argon atmosphere at a heating rate of 10K/s. X-ray Diffraction (XRD) was used to analyze the

Fig. 2 The nominal atomic percent compositions of the Al-Co-Ni alloys studied in this work

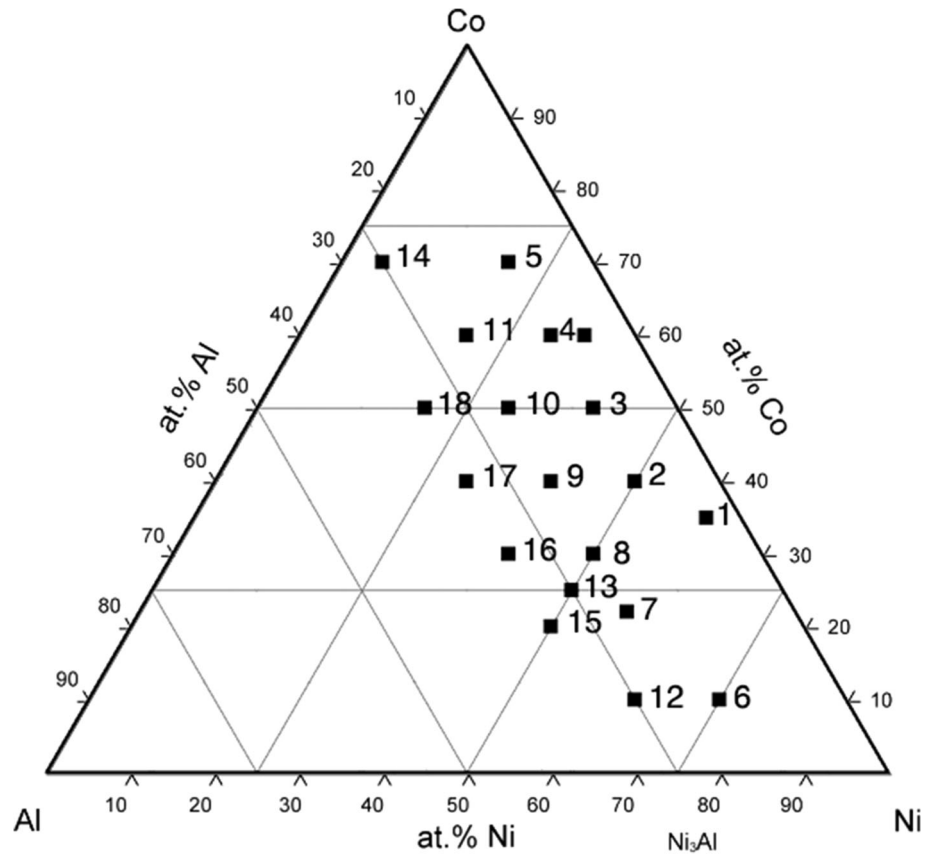


Table 1 Nominal composition and amount of cold work in Al-Co-Ni alloy samples

Alloy no.	Alloy nominal composition	Nominal composition, at.%			Amount of cold work, %	1100 °C annealing time, h
		Ni	Co	Al		
1	Ni61Co35Al4	61	35	4	50	94
2	Ni50Co40Al10	50	40	10	50	24
3	Ni40Co50Al10	40	50	10	50	24
4	Ni30Co60Al10	30	60	10	50	24
5	Ni20Co70Al10	20	70	10	50	24
6	Ni75Co10Al15	75	10	15	15	96
7	Ni58Co22Al20	58	22	20	8	96
8	Ni50Co30Al20	50	30	20	17	24
9	Ni40Co40Al20	40	40	20	15	24
10	Ni30Co50Al20	30	50	20	50	96
11	Ni20Co60Al20	20	60	20	50	24
12	Ni65Co10Al25	65	10	25	5	96
13	Ni50Co25Al25	50	25	25	5	94
14	Ni5Co70Al25	5	70	25	0	94
15	Ni50Co20Al30	50	20	30	0	n.a.
16	Ni40Co30Al30	40	30	30	0	n.a.
17	Ni30Co40Al30	30	40	30	0	n.a.
18	Ni20Co50Al30	20	50	30	0	n.a.

crystal structures of the phases present in the samples. The XRD spectra were obtained on a Thermo ARL θ - θ diffractometer using Cu-K α radiation. The GSAS II software package was used to refine the lattice parameters and phase fractions. Thermo-Calc with the TCNI8 database was used to calculate the isothermal sections.

3 Results and Discussion

3.1 Phase Equilibria

Based on the EDS analysis, the equilibrium compositions of β -(CoAl, NiAl), γ -(Co,Ni) and γ' -(Ni,Co)₃Al phases annealed at 1100 and 800 °C are listed in Tables 2 and 3. The corresponding isothermal sections are plotted in Fig. 3, 4, 6, 7, and 9. Three symbols are used to represent the different phases—the star is for Gamma (γ) phase; the half solid circle is for Gamma prime (γ') phase; the square is for Beta (β) phase, and the triangle is for the average measured composition of the alloys from EDS analysis, in which the solid triangle symbol represents the alloy composition with multiple phases while the empty triangle is for the alloy composition that is single-phase at that temperature.

3.1.1 Isothermal Section at 1100 °C

The results of our experimental investigation of the samples annealed at 1100 °C are shown graphically in Fig. 3,

superimposed on three previously reported isothermal sections of the Al-Co-Ni system at 1100 °C by Ref 13, 9, and 1.

From Fig. 3(a) it can be seen that the difference between the experimental data and the reported phase boundaries are significant. The two-phase region between γ and β phase is narrower as shown by the star and square symbols. The γ phase field boundary lies mainly along 14–17 at.% Al while the β phase field boundary is parallel to 34 to 36 at.% Al. The three-phase field ($\gamma' + \gamma + \beta$) which is indicated as a triangle in the isothermal section according to Jackson et al.'s results does not match the experimental data either. This consequently affects the γ' single phase field and the $\gamma' + \gamma$ two-phase field as well. Since the phase diagram by Jackson et al. contains many hypothetical field boundaries,^[13] the phase boundaries can not be considered accurate and this explains why there is significant difference between our experimental data and the published one. As a result, our present work is helpful in confirming and improving the accuracy of the phase diagram.

The isothermal sections shown in (Fig. 3b and c) are similar to each other and are closer in agreement with our experimental data. In both figures, the γ phase field boundary matches the experimental results. It can be seen that alloys 1–6 are in the γ single-phase region at 1100 °C. For the boundary of the β phase field, our experimental data matches Fig. 3(c) better except for the data point of alloy 14, which indicates that at higher Co amount the boundary is bending towards higher-Al content instead of

Table 2 Equilibrium compositions of β , γ and γ' phases in Al-Co-Ni alloys equilibrated at 1100 °C and overall alloy compositions determined using EDS

Alloy no.	Alloy nominal composition	Gamma (γ), at.%			Gamma prime (γ'), at.%			Beta (β), at.%			Alloy content, at.%		
		Ni	Co	Al	Ni	Co	Al	Ni	Co	Al	Ni	Co	Al
1	Ni61Co35Al4	60.0	35.5	4.5	60.0	35.5	4.5
2	Ni50Co40Al10	49.0	40.2	10.8	49.0	40.2	10.8
3	Ni40Co50Al10	39.3	50.1	10.6	39.3	50.1	10.6
4	Ni30Co60Al10	29.7	59.3	11.0	29.7	59.3	11.0
5	Ni20Co70Al10	19.8	69.5	10.7	19.8	69.5	10.7
6	Ni75Co10Al15	73.2	10.2	16.5	73.2	10.2	16.5
7	Ni58Co22Al20	55	25.6	19.3	58.2	17.8	24	56.6	21.9	21.5
8	Ni50Co30Al20	49.0	32.1	18.9	48.7	20.4	30.9	48.1	30.3	21.6
9	Ni40Co40Al20	38.6	43.4	17.8	40.9	28.1	31.0	39.1	39.8	21.1
10	Ni30Co50Al20	29.3	53.0	17.7	33.0	35.0	32.0	30.4	47.4	22.2
11	Ni20Co60Al20	18.0	65.0	17.0	22.3	45.4	32.3	19.2	59.1	21.7
12	Ni65Co10Al25	63.4	10.1	26.5	63.4	10.1	26.5
13	Ni50Co25Al25	49.4	32.6	18.0	50	20.2	29.8	48.2	24.7	27.1
14	Ni5Co70Al25	4.0	80.8	15.2	5.7	60.6	33.7	4.9	70	25.1

Table 3 Equilibrium compositions of β , γ and γ' phases in Al-Co-Ni alloys equilibrated at 800 °C determined using EDS

Alloy No.	Alloy nominal composition	Gamma (γ), at.%			Gamma prime (γ'), at.%			Beta (β), at.%			Average, at.%		
		Ni	Co	Al	Ni	Co	Al	Ni	Co	Al	Ni	Co	Al
1	Ni61Co35Al4	59.9	35.4	4.7	59.9	35.4	4.7
2	Ni50Co40Al10	48.7	40.1	11.2	48.7	40.1	11.2
3	Ni40Co50Al10	39.4	50.3	10.3	39.4	50.3	10.3
4	Ni30Co60Al10	29.4	59.6	11.0	29.4	59.6	11.0
5	Ni20Co70Al10	20.1	68.4	11.5	20.1	68.4	11.5
6	Ni75Co10Al15(a)	74.1	10.4	15.5
7	Ni58Co22Al20	57.3	32	10.7	59.3	18	22.7	57.4	22	20.6
8	Ni50Co30Al20	39.6	50	10.4	53.7	22.1	24.2	45.3	19.4	35.3	51	29.1	19.9
10	Ni30Co50Al20	28.4	56.3	15.3	35.3	29.3	35.4	30.2	47.1	22.7
11	Ni20Co60Al20	16.9	69.7	13.4	24.7	39.2	36.1	19.6	57.3	23.2
12	Ni65Co10Al25	65.4	10.1	24.4	65.4	10.1	24.4
13	Ni50Co25Al25	34.5	52.9	12.6	52.9	23.8	23.3	43.2	22.3	34.4	51.2	25.2	23.7
14	Ni5Co70Al25	3.9	85.3	10.8	6.4	52	41.6	4.6	74.7	20.7
15	Ni50Co20Al30	54.4	20.6	25	45.2	20.4	34.5	50.2	20	29.8
17	Ni30Co40Al30	22.4	63.1	14.5	30.3	33.7	36	28.5	39.1	32.4
18	Ni20Co50Al30	13.8	72.5	13.6	20.3	43.9	35.8	18.9	49.7	31.4

(a) The precipitate phase is too small in size to be determined quantitatively by EDS

lower Al-content. When it comes to the $\gamma' + \gamma + \beta$ three-phase field, our EDS results show that the three phase triangle should be located at higher Co content than shown in the previous work. As a result of this, the upper end of the γ' single-phase field should extend to greater Co solubility, higher than 18 at.%. Another difference lies in the γ' single-phase region, which should be shifted to higher Al content to include the composition of alloy 12 according to the experimental data.

From the comparison above, it could be seen that the existing isothermal sections by Hubert-Protopopescu et al. and Kainuma et al. are in reasonable agreement with our data while some areas have small discrepancies. In Fig. 4, our data are superimposed on the 1100 °C isothermal section calculated from the TCNI8 database using Thermo-Calc. It should be noted that in TCNI8, FCC_L12 represents the paramagnetic γ phase, FCC_L12#2 denotes the ordered γ (Ni_3Al) phase and FCC_L12#3, represents the ferromagnetic γ phase, which will appear in later figure and discussions. The calculated results show partial agreement with the experimental data in the low Al content region except for the γ single-phase field boundary and the two-phase field of $\gamma' + \beta$. In the recent published work by Ref 15 where Thermo-Calc is used based on first-principles calculations, the calculated results are in good agreement with the experimental results in this work.

In addition, the binary data were evaluated for comparison with the current experimental data. The calculated

Al-Co binary phase diagram reported by Ref 23 is shown in Fig. 5 (Solid lines), which shows minor discrepancies from the β phase boundary at 1100 °C. On the binary side of Al-Ni, comparison was also made with the evaluated diagram by Okamoto (supplementary Fig. S1).^[24] The binary end of the γ' single-phase region is seen to be in good agreement with the isothermal section in Fig. 3(c). At 1100 °C the binary Co-Ni phase diagram exhibits complete solid solubility.

Therefore, combining with previously published data by Ref 17, 24 and 23, the isothermal section of Al-Co-Ni in the Ni-rich region (<50 at.%Al) at 1100 °C could be established as shown in Fig. 6. From the diagram, it can be seen that the published data by Ref 17 near the Ni-Al binary end agree very well with the data by Ref 24 for the binary Ni-Al, and these are also in good accordance with the present experimental results.

3.1.2 Isothermal Section at 800 °C

After annealing at 800 °C for 2 weeks, all 18 alloys were analyzed with EDS. Figure 7 shows the published diagram by Ref 8 also including the experimental data from this work for comparison. It can be seen that the β phase field boundary is in excellent agreement with the published work as well as the $\gamma' + \beta$ two-phase region. However there is a significant difference in the position of the γ phase field boundary. From our experimental results, the

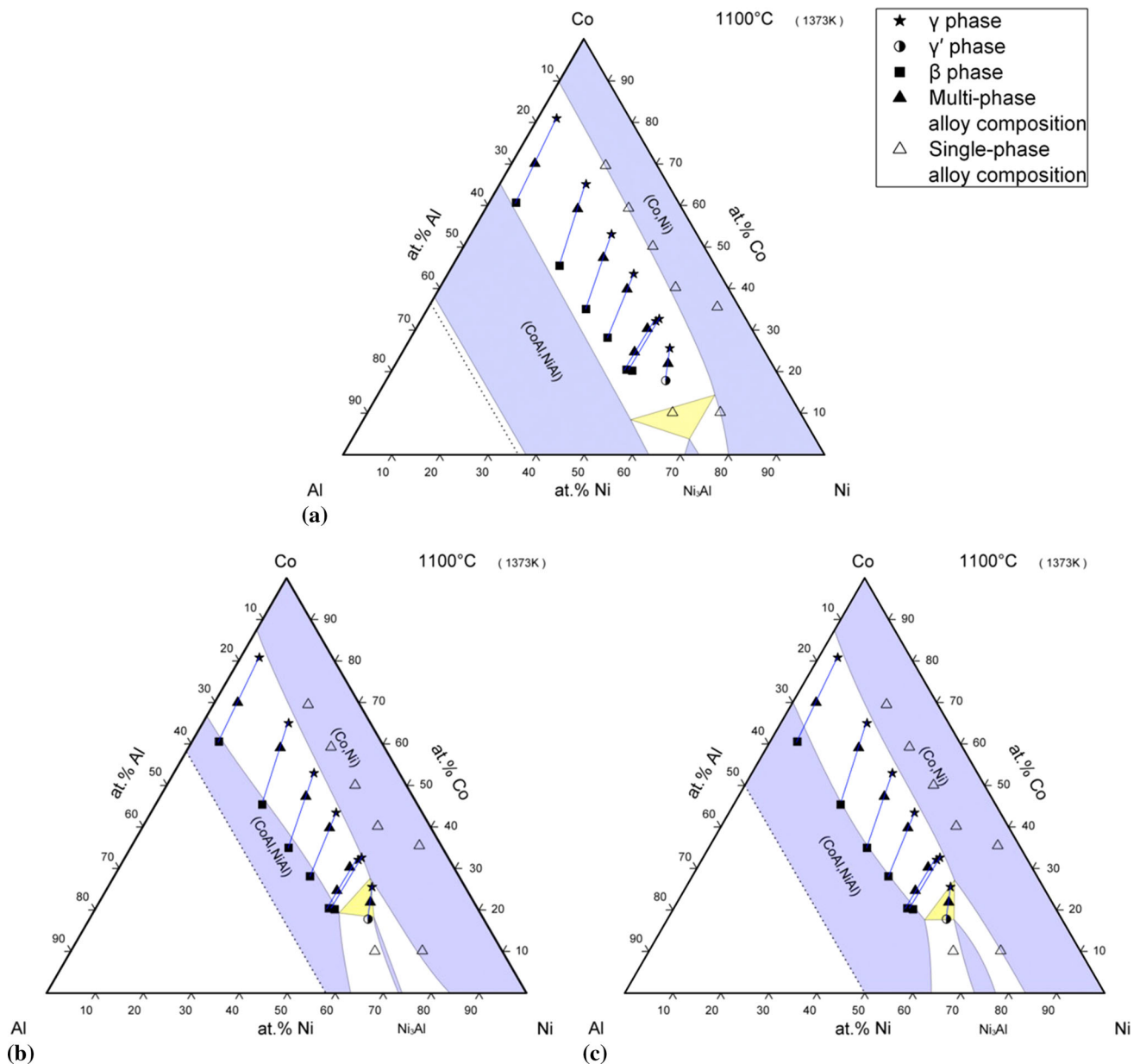


Fig. 3 Isothermal sections at 1100 °C in the Al-poor area adapted from SpringerMaterials and used with permission. The phase compositions determined in this work using EDS are superimposed on the published diagrams by (a) Ref 13; (b) Ref 9; (c) Ref 1

boundary is observed to be located at higher Al content, as shown in the figure. For the $\gamma' + \gamma + \beta$ three-phase region, we had two alloys Ni 30-20 and Ni 25-25, located in the three-phase field. These data indicate that the γ vertex is at lower Co content compared with the 800 °C isothermal section by Schramm, which makes the three-phase region smaller than on the previously reported diagram. The γ' single-phase field is in good agreement with our experimental results.

Similarly, the calculated isothermal section at 800 °C using Thermo-Calc (TCNI8 database) is shown in supplementary Fig. S2, with our experimental data superimposed

on it. Compared with the results in this work, significant difference can be seen between the calculated diagram and the experimental one. The three-phase field of $\gamma' + \gamma + \beta$ is actually shifted to lower Co content. Moreover, from the calculated isothermal section, there is a small two phase region extending into the γ single-phase region which corresponds to a γ_p paramagnetic/ γ_f ferromagnetic phase separation according to the calculated results. This region extends towards lower Co content on decreasing the temperature to 600 °C (supplementary Fig. S3). Since none of the initial alloy compositions lie in the *Nishizawa* horn region predicted by Thermo-Calc an additional alloy, Ni

Fig. 4 Isothermal section at 1100 °C superimposed on the calculated diagram using Thermo-Calc (TCNI8 database)

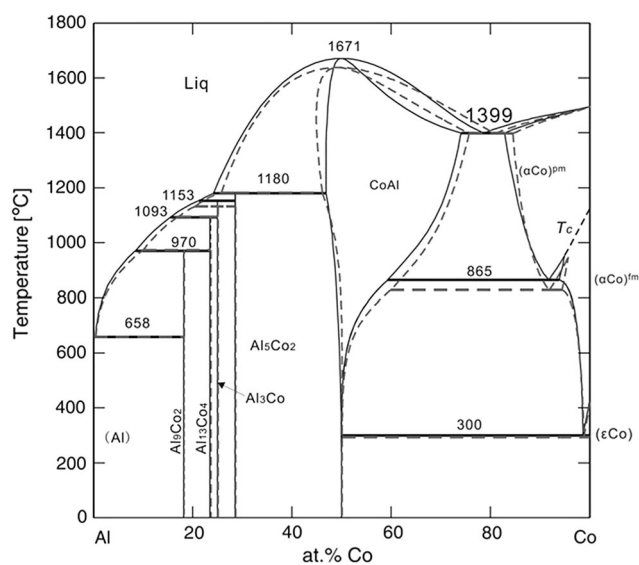
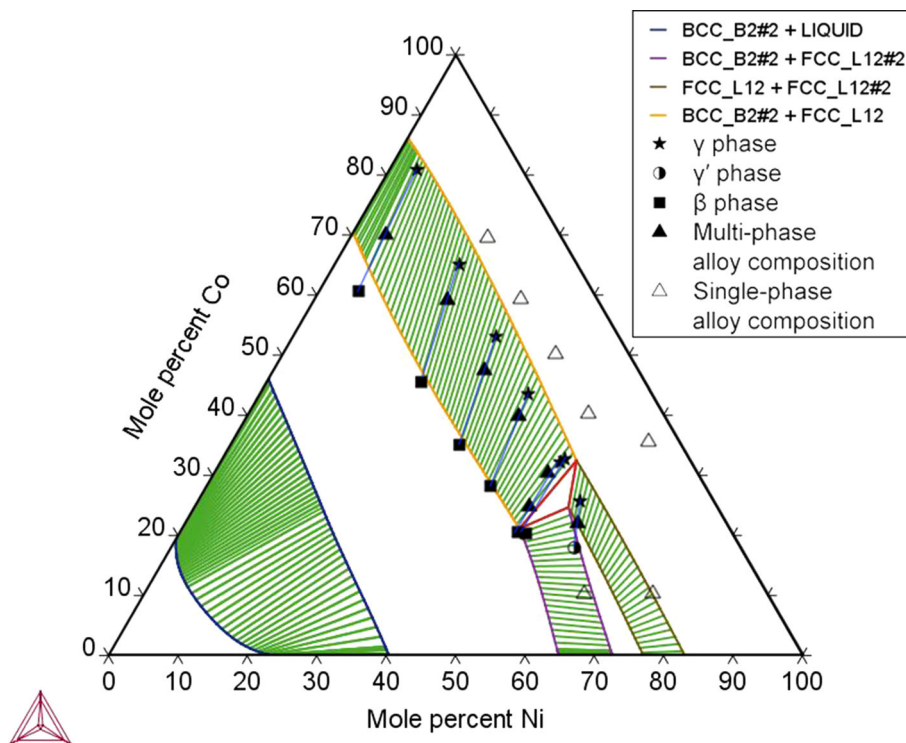


Fig. 5 The published Al-Co binary phase diagram by Stein et al. shows a *Nishizawa* horn at high Co content^[23] used with permission from Elsevier

35-4 (Alloy No.1) was produced and heat treated at 600 °C for 2 weeks. This should place it in the two-phase *Nishizawa* horn region (Fig. S3), where the predicted composition difference between the phases should manifest itself in the alloy properties. However, from EDS, XRD, hardness tests and optical microscope observations, the predicted phase separation to $\gamma_p + \gamma_f$ was NOT observed. A *Nishizawa* horn is predicted to occur in the Co-Al binary system

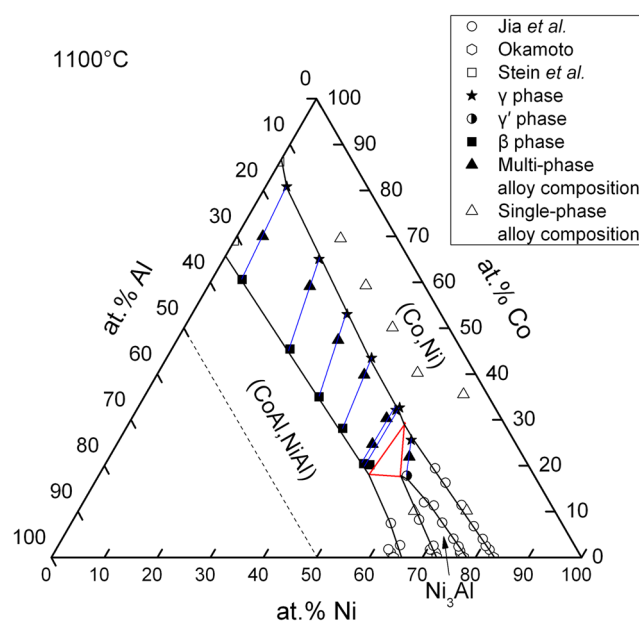
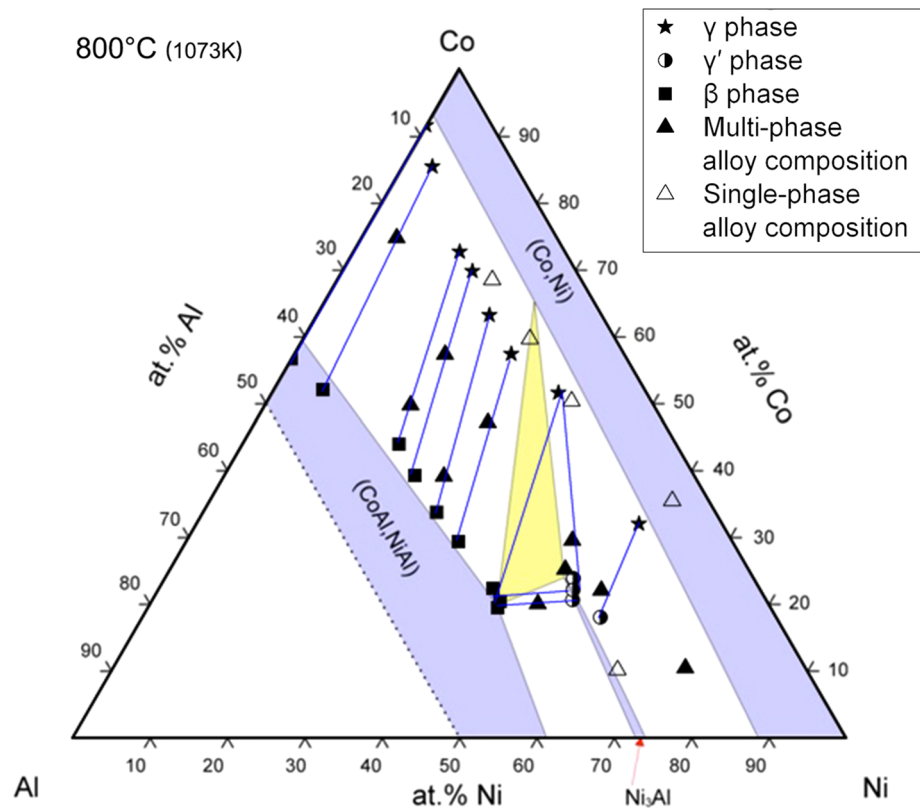


Fig. 6 Isothermal section at 1100 °C established in this work

(Fig. 5)^[23] and the one predicted in the ternary system appears to be an extension from the binary system. However, the Thermo-Calc calculations we have performed show that it is not predicted to be stable in the ternary system at high Cobalt content. This suggests that some parameter adjustment in the TCNI8 database may be needed if the *Nishizawa* horn is indeed stable in the binary Al-Co diagram. It should be noted that what appears to be a

Fig. 7 Isothermal section at 800 °C based on the published diagram by Ref 8 adapted from SpringerMaterials and used with permission. The phase compositions determined using EDS in this work are superimposed on the section



single three-phase region, $\gamma' + \gamma + \beta$, in Fig. S2 must in fact have a second, narrow three-phase region $\gamma' + \gamma_p + \gamma_f$. It appears that 800 °C is close to the calculated four phase equilibrium temperature corresponding to $\gamma' + \beta + \gamma_p + \gamma_f$.

As mentioned above, from the calculated isothermal section from Thermo-Calc, the *Nishizawa* horn starts to occur as the temperature drops to 832 °C. Fig. S2 and S3 show that the horn-shape area is seen to start at the high Co content region and extends towards lower Co content on decreasing the temperature to 600 °C. Although it was impossible to generate the appropriate isothermal sections that show the phase equilibria as a function of temperature in this region, the transition in phases relating to the *Nishizawa* horn with a decrease in temperature is shown schematically in Fig. 8, from which a transition reaction relating 4 phases could be obtained; $\beta + \gamma_p \rightarrow \gamma' + \gamma_f$. The $\beta + \gamma_p + \gamma_f$ phase field must exit the ternary at the Al-Co binary side at the eutectoid temperature.

Similarly, based on published data, the 800 °C isothermal section of Al-Co-Ni in the Ni-rich region was constructed as shown in Fig. 9. It can be seen that the γ single-phase region based on our data is observed to tend towards higher Al content, compared with the diagram by Ref 8, wavelength dispersive spectroscopy data from Ref 16 and calculated results from Thermo-Calc. The γ' single phase and $\beta + \gamma'$ two-phase areas together with the Al-Ni binary

end are confirmed with reasonable agreement with published data. However, for the Al-Co binary end, experimental data from a Co-30 at.%Al sample annealed at 800 °C, which we used to determine the phase boundaries, agrees with Ref 23 data on the β phase boundary but exhibits significant discrepancy at the γ phase boundary. It is not yet clear if the difference comes from the phase separation of paramagnetic/ferromagnetic γ phases according to the calculated data by Ref 23, which predicts the occurrence of a *Nishizawa* horn.

Since at 800 °C the only previously published isothermal section is from the work by Ref 8, which was not based on direct measurement of phase compositions, the present experimental results are more reliable.

3.2 Liquidus Projection

After arc-melting, the alloys were polished and observed using optical microscopy and the primary phase and eutectic compositions were determined using EDS. The as-cast microstructures are arranged in order of increasing Al composition. Fig. 10 shows the variation of as-cast microstructure from low Al (4 at.%) content to high Al content (30 at.%). It can be seen that when the Al content is lower than 15 at.%, only chemical segregation is observed within the grains and the grain boundaries are clearly observable as shown in Fig. 10(a)-(c). The grain size also

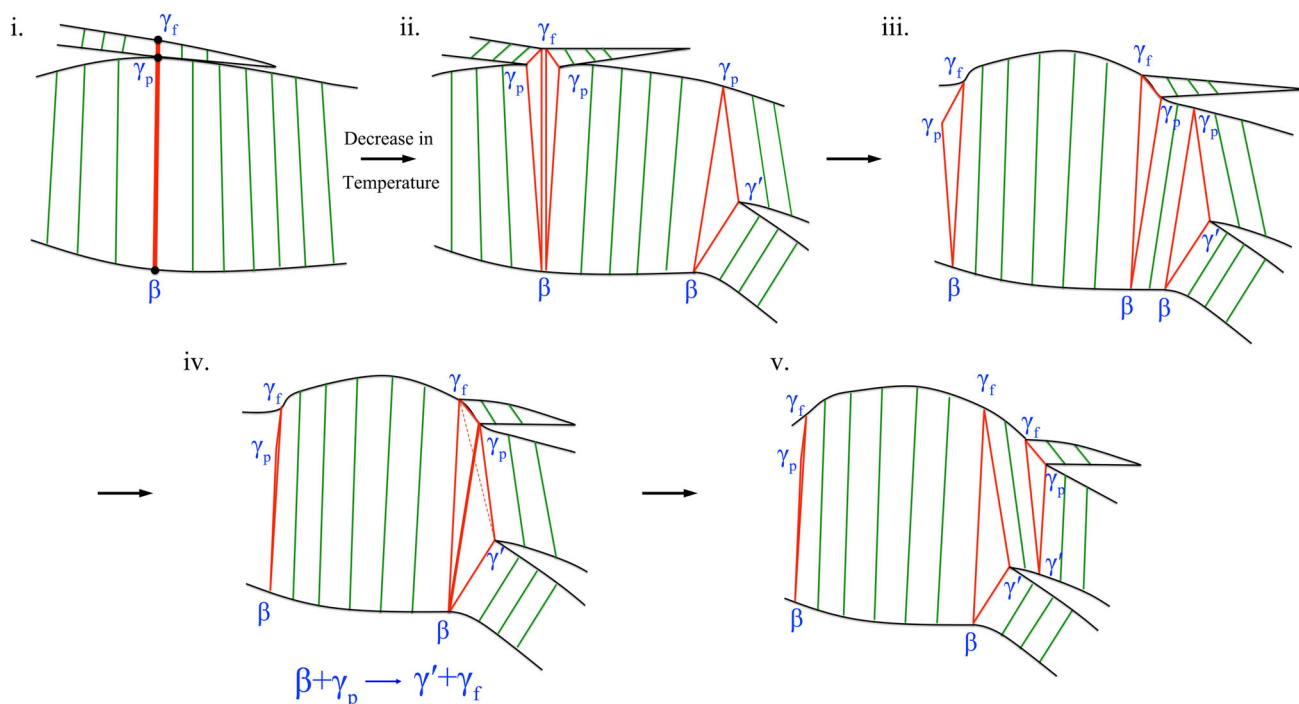


Fig. 8 The phase transition relating to the *Nishizawa* horn with decrease in Temperature

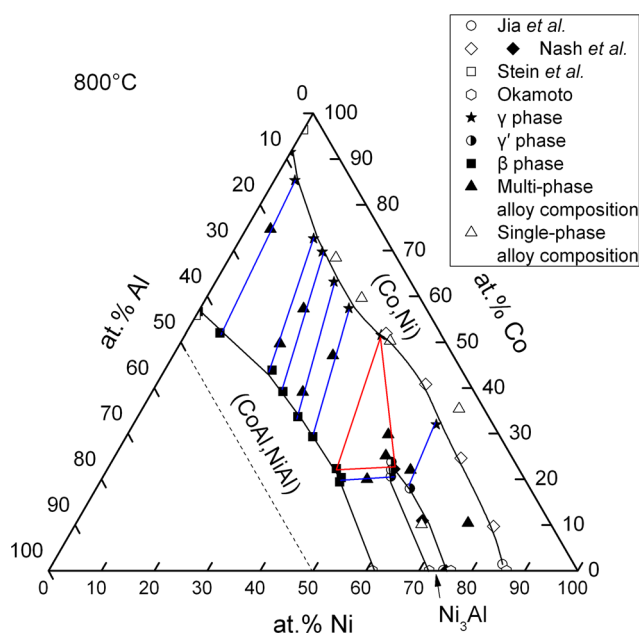


Fig. 9 Isothermal section at 800 °C established in this work

varies as the composition changes. When Al content increases to 20 at.%, distinct dendrites appear and in the interdendritic regions there is a eutectic structure, as shown in Fig. 10(d), (e). With Al content increasing to 25 at.%, in Fig. 10(f) and g), not only is a eutectic structure observed, but within the β phase dendrites, a martensite structure appears as indicated within the circle in Fig. 10(g). Finally,

when the Al content is increased to 30 at.%, Fig. 10(h), (i), the eutectic structure disappears. Plate-like martensite still exists in alloy 15, Ni 20–30, with a small amount of a light contrast phase between the grain boundaries. In alloy 18, Ni 50–30, Fig. 10(i), cored dendrites were observed, which were determined to be β phase by EDS as expected due to high Al content.

Analyzing the average composition of the eutectic structure in the as-cast microstructures in Fig. 10, provides approximate compositions corresponding to the monovariant liquidus line as shown in Fig. 11. Such measurements are approximate because the measurement is averaging two phases and the sampled region may not be representative of the phase fractions, also the regions are usually quite small so it is possible that x-rays may be sampled from the primary phase as well as the eutectic structure. Figure 11 shows the experimental compositions determined in this work superimposed on the published liquidus projection for the Al-poor composition region by Ref 8, as well as the change in as-cast microstructure of alloys with different compositions. It can be seen that the experimental data are in good agreement with the liquidus line determined by Ref 8.

In addition, DSC analysis was performed on selected samples with compositions close to the liquidus line to determine the solidus temperature. Supplementary Fig. S4 shows a typical DSC heat flow versus sample temperature curve during the heating process. It can be seen that a significant endothermic peak appeared with an onset

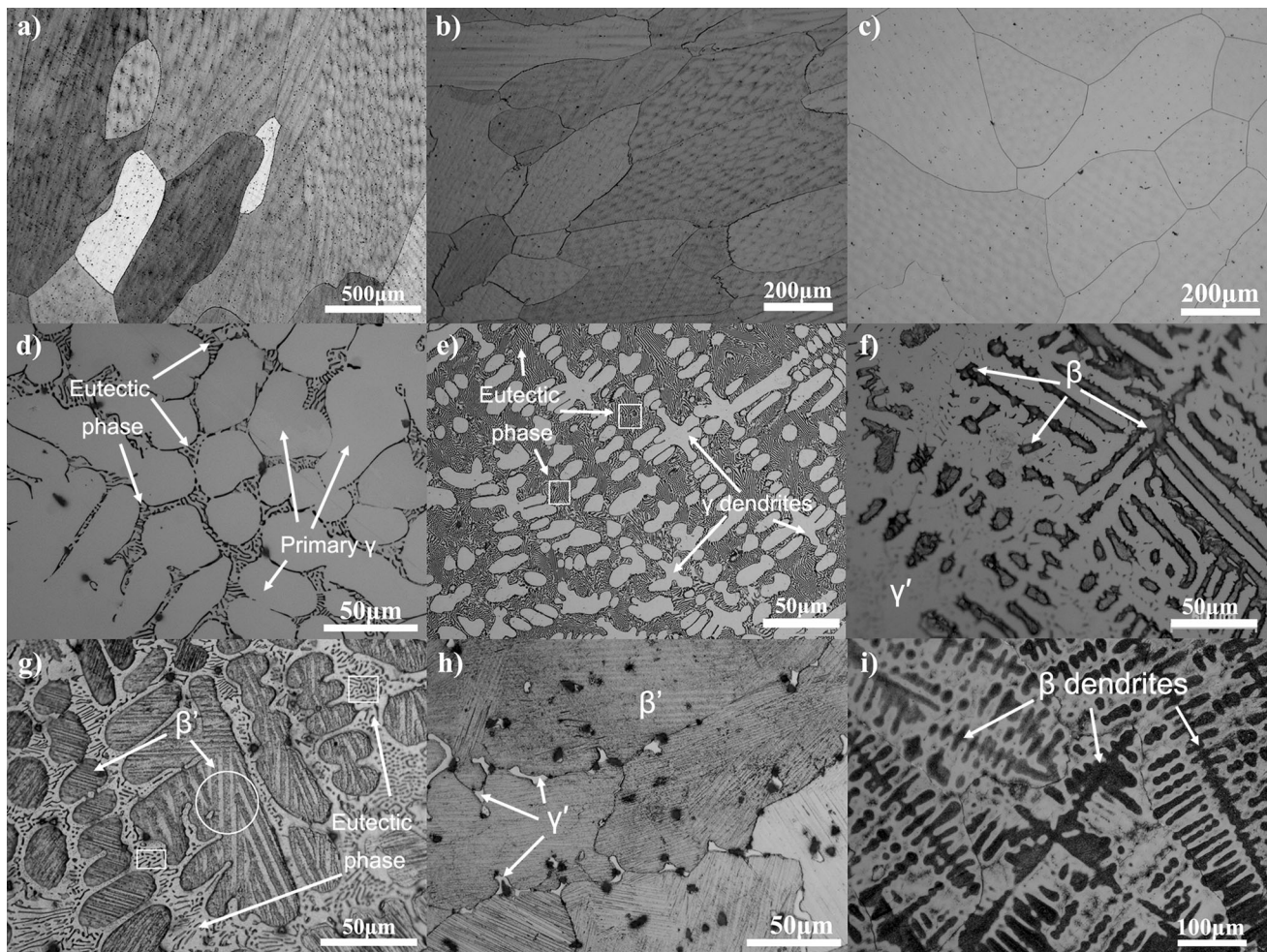


Fig. 10 Optical microstructure of as-cast alloys (a) No. 1: Ni 35-4; (b) No. 2: Ni 40-10; (c) No. 6: Ni 10-15; (d) No. 7: Ni 22-20; (e) No. 11: Ni 60-20; (f) No. 12: Ni 10-25; (g) No. 13: Ni 25-25; (h) No. 15: Ni 20-30; (i) No. 18: Ni 50-30

temperature of 1374 °C. Another peak occurred at 663.9 °C which corresponds to the Curie transformation temperature of γ . Table 4 lists the determined solidus temperatures of the Al-Co-Ni samples, which was observed to decrease with a decrease in Co content. The measured data also indicate the direction of decreasing temperature, which is in agreement with the isotherms in Fig. 11.

Therefore, from the above microstructure evolution, with decreasing Co content from 60 at.% to 10 at.%, the as-cast structure changes from mostly eutectic structure between the dendrites to peritectoid structures as shown in the lower left corner of Fig. 11. This indicates that the three-phase triangle (liquid + γ + β) rotates with decreasing temperature, changing the solidification character from eutectic to peritectic. According to the binary phase diagrams the invariant reaction temperature in the Al-Co system^[23] is 1399 °C ($L \rightarrow \gamma + \beta$) and in the Al-Ni system^[24] are 1362 °C ($L + \gamma \rightarrow \gamma'$) and 1360 °C ($L \rightarrow \beta + \gamma'$). Based on Schramm's^[8] work there is a four-phase transition reaction ($L + \gamma \rightarrow \gamma' + \beta$) in the ternary

system close to the NiAl binary side and the rotation of the ($L \rightarrow \gamma + \beta$) phase field as Co content decreases is consistent with this observation.

3.3 Microstructure Evolution

After determining the isothermal sections at 1100 and 800 °C, the microstructural evolution of alloys with different compositions was studied systematically with decreasing temperature as shown in Fig. 12. Four typical alloys with Al composition varying from 10 to 30 at.% were analyzed with optical microscopy and BSC imaging. From Fig. 12(a)-(c), at low Al content, 10 at.%, after 1100 °C homogenization for 24 h, the chemical segregation disappeared and the resulting microstructure exhibits large grains with twins inside. In alloy 5, Ni 70-10, it could be seen that after annealing at 1100 and 800 °C, the alloy is single γ phase, in accordance with the EDS results (Fig. 12a, b). While when aged at 600 °C for 4 weeks, after etching, plate-like γ' discontinuous precipitation (DP) from

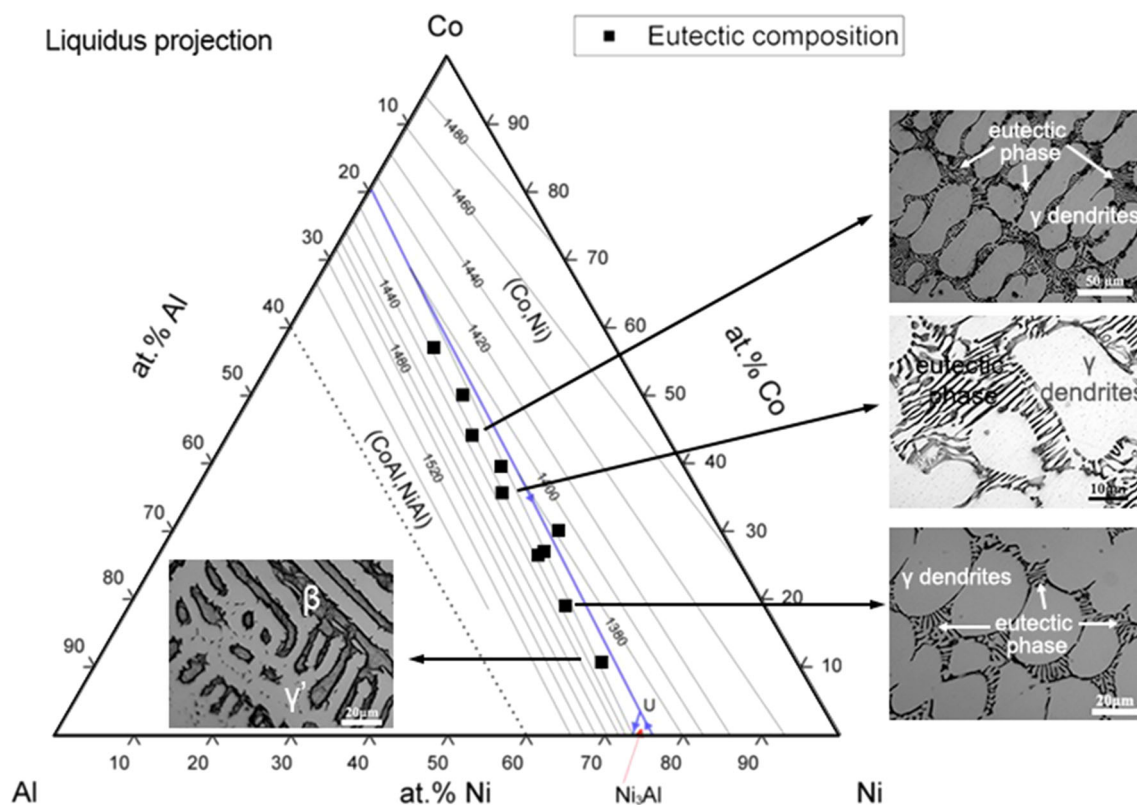


Fig. 11 Liquidus projection of Al-Co-Ni system in the Al-poor composition region by Schramm superimposed with interdendritic region compositions determined in this work using EDS,^[8] adapted from SpringerMaterials and used with permission

Table 4 The determined melting points of selected Al-Co-Ni samples

Sample	Melting point, °C
Ni70-25	1376
Ni60-20	1374
Ni50-20	1369
Ni40-20	1364
Ni25-25	1364
Ni10-25	1359

the γ matrix was observed as shown in Fig. 12(c). A film of discontinuous $\gamma + \gamma'$ precipitation was seen to occur along the grain boundaries. This is consistent with previous work that indicated a propensity for discontinuous precipitation of $\gamma + \gamma'$ with increasing Co content and decreasing temperature.^[25]

When the Al content is 30 at.%, alloy 18, as shown in Fig. 12(d), at 1200 °C, the alloy was single phase β . After annealing this alloy at 800 °C, small precipitates of γ have formed in the β matrix, Fig. 12(e). The precipitates are very small in size so that it is not clear by optical microscopy. The precipitation could also be inferred from the increased rough surface of the grains after etching. When the annealing temperature is 600 °C, at a higher

magnification, needle-like precipitates of γ phase could be observed in the matrix, Fig. 12(f).

From the above results, it can be seen that alloys 5 and 18, with low Al (10 at.%) and high Al content (30 at.%) respectively, are both single phase at high temperature but have a second-phase precipitation when annealing at lower temperatures. This indicates decreasing solubility with decreasing temperature for both γ and β phases. The next two alloys in Fig. 12 have an Al composition between 20 and 25 at.%, which produces a more complex structure than the above two alloys, as shown in the BSC images, Fig. 12(g)–(l). In alloy 11, Ni 60-20, compared with the as-cast structure in Fig. 10(e), the eutectic structure was removed after homogenization and high temperature annealing at 1100 °C, resulting in a two-phase structure ($\beta + \gamma$), as indicated in Fig. 12(g). In composition-mode of backscattered electron imaging, the γ phase has lighter contrast due to the lower Al content, resulting in a higher average atomic number than for the β phase. When annealing at 800 °C, it is seen that within both phases, a second-phase appears, which is explained as precipitation of β -phase in γ phase and vice versa, Fig. 12(h), consistent with both single-phase boundaries decreasing in solubility with decreasing temperature. The microstructure is also in good agreement with the previous isothermal section

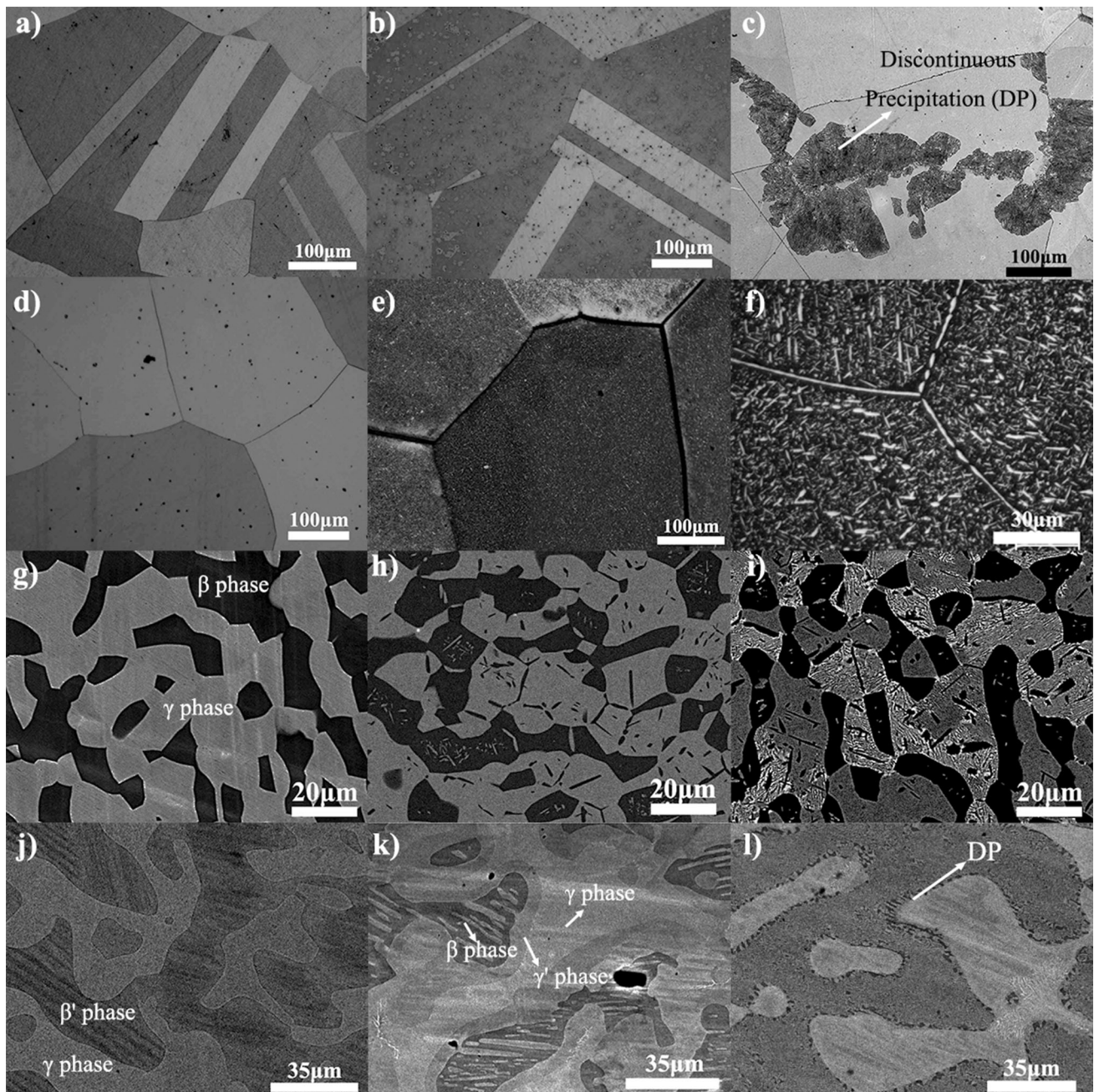


Fig. 12 Microstructure evolution of alloys No. 5, 18, 11 and 13: Optical images of alloy No. 5: Ni 70-10, equilibrated at (a) 1100 °C, (b) 800 °C and (c) 600 °C; of alloy No. 18: Ni 50-30, equilibrated at (d) 1200 °C, (e) 800 °C and (f) 600 °C; Back Scattered electron

Composition mode images of alloy No. 11: Ni 60-20, equilibrated at (g) 1100 °C, (h) 800 °C and (i) 600 °C; alloy No. 13: Ni 25-25, equilibrated at (j) 1100 °C, (k) 800 °C and (l) 600 °C

experimental results indicating a two-phase structure at this temperature. Subsequently, after 600 °C annealing, a third-phase γ' was seen to precipitate out discontinuously from the γ phase regions as shown Fig. 12(i).

Finally, in alloy 13, the equilibrated microstructures are shown in Fig. 12(j)–(l). From the 1100 °C isothermal section, this alloy is seen to fall in a two-phase field and the microstructure shows the two phases ($\gamma + \beta'$) accordingly.

The two phases are marked as shown in Fig. 12(j), which can be inferred by the variance in contrast caused by different atomic numbers under compositional backscattered mode in the SEM. When annealing at 800 °C, Fig. 12(k), the three phases are quite obvious, where the γ' lies around the dark β phase due to a peritectoid reaction $\gamma + \beta \rightarrow \gamma'$. The β phase no longer exhibits a martensitic structure since its equilibrium composition at this temperature is different

from that at 1100 °C (see Tables 2 and 3). After the alloy was annealed at 600 °C, Fig. 12(i), it can be seen that similarly, a certain amount of secondary- γ phase is coming out from the primary β phase, and γ' phase is also precipitating out from the γ matrix discontinuously as indicated in the image, making the microstructure even more complex. It is also probable that γ' is precipitating continuously in the γ matrix region but on a scale not observable under these imaging conditions.

In summary, from the microstructure evolution of the four alloys selected, a general conclusion can be made: the high temperature homogenization treatment employed removes the dendritic and eutectic structures and chemical segregation; secondary phases precipitate out from the primary phase on annealing at lower temperatures. Both the optical microscopy and BSC observation confirm the experimentally determined isothermal sections based on EDS data.

3.4 Martensitic Transformation

According to Ref 1 and 26, who investigated the martensitic transition starting temperature M_s , they confirmed that in high Co alloys with more than 30 at.%, martensitic transformation was seen to occur and M_s decreases with increasing Co and Al content as well as increasing annealing temperature. In this work, as shown in Fig. 12(j), plate-like β' martensite phase is observed in Ni 25-25, since the sample was quenched from 1100 °C. The crystal structure was confirmed by XRD as discussed in section 3.6. Besides, the sample Ni 30-20 and Ni 20-30 also exhibit martensite structure after annealing at 1100 and 1200 °C, respectively followed by quenching, which is shown in supplementary Fig. S5. No martensite structure was found in other samples with 20 at.% and 30 at.%Al. From the summary data in Ref 26, when Co and Al compositions increase to higher than 30 at.%Co and 30 at.%Al, M_s drops below room temperature, so it will not be detected unless the sample is quenched in liquid nitrogen or even lower temperature.

From the above discussion, the results in the present work are seen to be in good agreement with the previous studies.

3.5 Hardness Test

The room temperature hardness of the alloy samples equilibrated at different temperatures is summarized as shown in supplementary Table S1. It can be seen in the table that for Ni 35-4, the hardness does not change with decreasing annealing temperature. It remains almost the same at around 116HV with small standard deviations. This suggests the alloy remains single phase and does not

undergo a phase separation into ferromagnetic and paramagnetic phases. As Al content increases to 10 at.%, all four samples exhibit the same change in hardness values, which remain similar after 1100 and 800 °C annealing and increase significantly after annealing at 600 °C to twice the hardness value of the higher temperature annealing. This indicates precipitation hardening occurring at 600 °C, which means that the alloy composition falls in a single phase region at 1100 and 800 °C while it enters a two phase-region when the temperature is decreased to 600 °C. The microstructural observations discussed above also correlate with the hardness increase. As Al content keeps increasing, some of the alloys tend to have a similar hardness increase as the Al 10 at.% samples–Ni 40-20, Ni 50-20, Ni 60-20, Ni 25-25.

For samples with 30 at.%Al content, a hardness decrease was found in the predominantly β phase samples Ni 30-30, Ni 40-30 and Ni 50-30 annealed at 800 °C. Since all the samples were quenched from the isothermal annealing temperatures, lower hardness at lower annealing temperatures may be explained as resulting from a lower vacancy concentration since it is well known that vacancy hardening exists in intermetallic compounds.^[27,28] It is also possible that some greater degree of long range order may be achieved at even lower temperature, which might explain the increased hardness for the Ni 40-30 and Ni 50-30 samples annealed at 600 °C compared to 800 °C.

The hardness test summary from the table above indicates that at low Al content, the samples tend to be single phase at high temperatures with low hardness values. While as the Al content increases, due to the increasing amount of β phase, the hardness increases gradually to a high value. In addition, upon annealing at low temperature, 600 °C, the hardness usually increases significantly due to the precipitation from the matrix. The microstructure evolution discussed in the previous sections is in accordance with the hardness test results.

3.6 Lattice Parameters of Solid Phases

After analyzing the microstructure of samples under different heat-treatment conditions, XRD was performed on the characterized samples. Figure 13 shows the typical XRD pattern changes as the sample Ni 25-25 was annealed at different temperatures. For comparison, CrystalMaker® (CrystalMaker Software Limited, Oxfordshire, UK) was used to define the standard crystal structure unit cell and the standard powder diffraction patterns were generated by CrystalDiffract® accordingly as shown in Fig. 14. The General Structure Analysis System (GSAS) II software package^[29] was used to determine the lattice parameters of the phases present in each sample. The Crystallographic Information Files (CIF) of the four phases were obtained

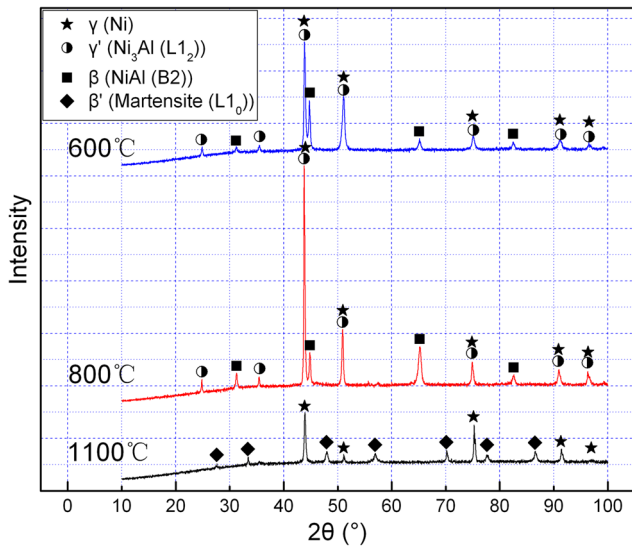


Fig. 13 XRD patterns of Ni 25-25 annealed at different temperatures compared with the calculated results

from Pearson’s Crystal Database with the entry numbers and references: γ (Ni) —1822334,^[30] γ' (Ni_3Al ($L1_2$))—1815423,^[31] β (NiAl ($B2$))—1010999,^[32] β' (Martensite ($L1_0$))—1932023,^[33] respectively.

The phase transformation process of Ni 25-25 could thus be inferred from the XRD results with reference to the standard XRD patterns shown in Fig. 14. At 1100 °C, two phases were detected in the alloy: γ and β' . This corresponds to the microstructure observation and EDS analysis. Since the sample was quenched from 1100 °C, a martensite ($L1_0$) structure is expected to be formed. The microstructure (both optical microscope and SEM) shows the plate-like morphology of the β' phase. However, from EDS results we can only determine the phase composition of the β' phase, the crystal structure (whether it is normal β or the martensite β') cannot be determined. While the XRD result clearly indicates the presence of β' phase and thus confirmed the martensitic transformation in Ni 25-25 when quenching from 1100 °C.

After annealing at 800 °C, a significant change in the XRD pattern could be seen, combining with the analysis from GSAS refinement, a third phase γ' appeared, but was overlapped with the γ fundamental peaks at certain 2θ positions. The peaks changed from those of γ and β' phases to γ , γ' and β . This is in accordance with the EDS analysis result. The superlattice peaks of $(001)_{\gamma'}$ and $(110)_{\gamma'}$ are intense enough to be detected, which also suggests the

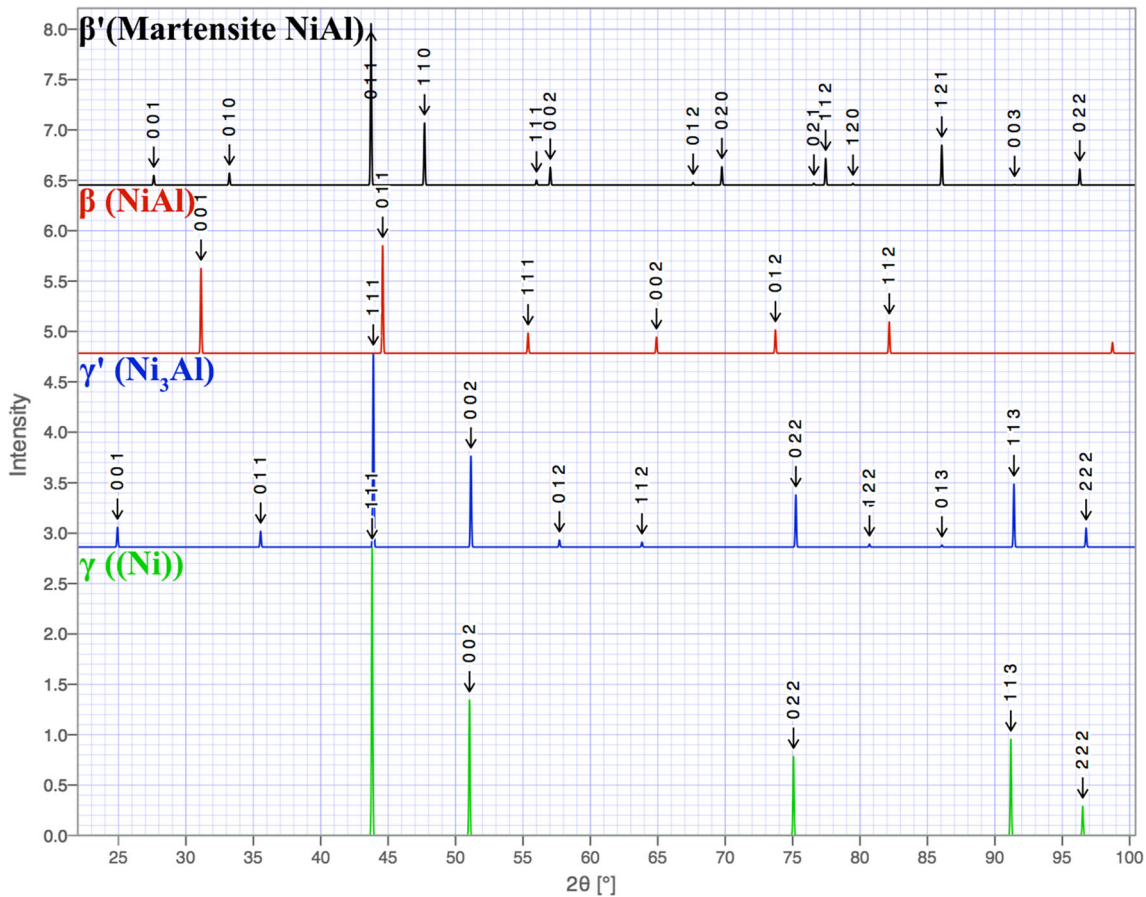


Fig. 14 Standard powder diffraction x-ray patterns of selected phases in the Al-Co-Ni system generated by CrystalDiffract®

Table 5 Lattice parameters of phases in Al-Co-Ni alloys at different annealing temperatures obtained by GSAS refinement

Samples	1100 °C, Å			800 °C, Å			
	γ	β	β'		γ	γ'	β
			a	c			
Ni50Co40Al10	3.55237				3.56417		
Ni40Co50Al10	3.56655				3.56446		
Ni30Co60Al10	3.56516				3.56567		
Ni20Co70Al10	3.56668				3.56611		
Ni50Co30Al20	3.56666		2.69403	3.22514	3.56857	3.58241	(a)
Ni40Co40Al20	3.56944		2.69391	3.22744	3.56636		2.85951
Ni30Co50Al20	3.57072		2.69633	3.19049	3.56695		2.85892
Ni20Co60Al20	3.57127	2.85719			3.56458		2.85835
Ni50Co25Al25	3.5698		2.68148	3.23298	3.58087	3.58570	2.86132
Ni50Co20Al30		3.56413	(a)
Ni40Co30Al30	3.56308		(a)
Ni30Co40Al30	3.56678		2.83321
Ni20Co50Al30	3.56639		2.871

(a) Diffraction peaks not detectable, but the phase was observed from SEM

phase fraction of γ' is significant. The presence of both γ and γ' gives overlapping fundamental peaks and so the presence of both is difficult to establish. When the annealing temperature was decreased to 600 °C, the diffraction peaks of γ , γ' and β phases were also detected as in the 800 °C sample. From the microstructure observation, a second γ' phase with lamellar structure precipitated from the β phase, which was distributed homogeneously but very small in size preventing accurate determination of the composition by EDS analysis.

The GSAS refinement was used to determine the lattice parameters of phases in Al-Co-Ni samples at different annealing temperatures 1100 and 800 °C. The results are shown in Table 5 below. For the lattice parameters the variation is based on composition of Al and Co with addition of Al leading to a larger increase in lattice parameter than addition of Co to Ni, which is consistent with the results of Ref 34.

4 Conclusions

In this work, the phase equilibria among γ , γ' , β and β' phases in the Al-Co-Ni system were determined experimentally. The partial isothermal sections at 1100 and 800 °C as well as a partial liquidus projection determined here result in modifications to previously published work. Through the microstructure evolution as a function of temperature, we can see that, cold work followed by homogenization is effective in removing the dendritic and eutectic structures and chemical segregation in as-cast alloys. At lower temperatures, 800 and 600 °C, second

phases will tend to precipitate out from the primary phases. Comparing the experimental results with the calculated results using Thermo-Calc (TCNI8), there is reasonable agreement. The predicted separation of the γ phase into a two-phase ferromagnetic and paramagnetic region has never been observed experimentally in this or other published work. However, the observation of such a region is not straightforward and is unlikely to be observed serendipitously without some prior knowledge as is provided by Thermo-Calc. Future work should explore the ferromagnetic and paramagnetic phase separation, as predicted using Thermo-Calc, to verify its occurrence in this system.

Acknowledgments This work was performed under National Science Foundation Grant DMR 1607943. One of the authors, Yang Zhou is grateful for the financial support from Chinese Scholarship Council. We are grateful for discussions with Suzanne Fries and Natalie Dupin regarding the Nishizawa horn originating in the Al-Co phase diagram.

References

1. R. Kainuma, M. Ise, C.-C. Jia, H. Ohtani, and K. Ishida, Phase Equilibria and Microstructural Control in the Ni-Co-Al System, *Intermetallics*, 1996, **4**, p S151-S158
2. Y. Tanaka, T. Ohmori, K. Oikawa, R. Kainuma, and K. Ishida, Ferromagnetic Co-Ni-Al Shape Memory Alloys with $\beta + \gamma$ Two-Phase Structure, *Mater. Trans.*, 2004, **45**(2), p 427-430
3. K. Oikawa, T. Ota, F. Gejima, T. Ohmori, R. Kainuma, and K. Ishida, Phase Equilibria and Phase Transformations in New B2-type Ferromagnetic Shape Memory Alloys of Co-Ni-Ga and Co-Ni-Al Systems, *Mater. Trans.*, 2001, **42**(11), p 2472-2475
4. J. Liu and J.G. Li, Microstructure, Shape Memory Effect and Mechanical Properties of Rapidly Solidified Co-Ni-Al Magnetic

- Shape Memory Alloys, *Mater. Sci. Eng. A*, 2007, **454–455**, p 423–432
5. Y. Xu, S. Kameoka, K. Kishida, M. Demura, A. Tsai, and T. Hirano. Catalytic Properties of Ni₃Al Intermetallics for Methanol Decomposition, *Mater. Trans.*, 2004, **45**(11), p 3177–3179
 6. Y. Zhou, P. Nash, T. Liu, N. Zhao, and S. Zhu, The Large Scale Synthesis of Aligned Plate Nanostructures, *Sci. Rep.*, 2016, **6**(1), Art. No. 29972. doi:[10.1038/srep29972](https://doi.org/10.1038/srep29972)
 7. V. Raghavan, Al-Co-Ni (Aluminum-Cobalt-Nickel), *J. Phase Equilib. Diffus.*, 2006, **27**(4), p 372–380
 8. J. Schramm, The Nickel-Cobalt-Aluminum Ternary System, *Z Metallkd*, 1941, **33**, p 403–412, in German
 9. M. Hubert-Protopenescu and H. Hubert, Aluminum-cobalt-nickel, *Ternary Alloys*, Vol 4, G. Petzow and G. Effenberg, Ed., VCH Verlagsgesellschaft, Weinheim, 1991, p 234–244
 10. K. Enami and S. Nenno, Memory Effect in Ni-36.8 At. Pct Al Martensite, *Metall. Trans.*, 1971, **2**(5), p 1487
 11. Y.L. Yang, Z. Shi, Y.S. Luo, Y. Lu, S.Y. Yang, J.J. Han, W.B. Li, C.P. Wang, and X.J. Liu, Interdiffusion and Atomic Mobility Studies in Ni-Rich fcc Ni-Co-Al Alloys, *J. Phase Equilibria Diffus.*, 2016, **37**(3), p 269–276
 12. L. Kaufman and H. Nesor, Calculation of Superalloy Phase Diagrams: Part IV, *Metall. Trans. A*, 1975, **6**(11), p 2123–2131
 13. M. Jackson and J. Rairden, Protective Coatings for Superalloys and the Use of Phase Diagrams, *NBS Spec. Publ.*, 1978, **496**, p 423–439
 14. P. Villars, A. Prince, and H. Okamoto, Al-Co-Ni, *Handb. Ternary Alloy Phase Diagr. ASM Int. Mater. Park OH*, 1995, **3**, p 3052–3063
 15. X.L. Liu, G. Lindwall, T. Gheno, and Z.-K. Liu, Thermodynamic modeling of Al-Co-Cr, Al-Co-Ni, Co-Cr-Ni Ternary Systems Towards a Description for Al-Co-Cr-Ni, *Calphad*, 2016, **52**, p 125–142
 16. C.K.L. Davies, P. Nash, and R.N. Stevens, Precipitation in Ni-Co-Al Alloys, *J. Mater. Sci.*, 1980, **15**(6), p 1521–1532
 17. C.C. Jia, K. Ishida, and T. Nishizawa, Partition of Alloying Elements Between γ (A1), γ' (L12), and β (B2) Phases in Ni-Al Base Systems, *Metall. Trans. Phys. Metall. Mater. Sci.*, 1994, **25**(3), p 473–485
 18. T. Nishizawa, M. Hasebe, and M. Ko, Thermodynamic Analysis of Solubility and Miscibility Gap in Ferromagnetic Alpha Iron Alloys, *Acta Metall.*, 1979, **27**(5), p 817–828
 19. K. Hack, I.2—Models and Data, *The SGTE Casebook Thermodynamics at Work*, 2nd ed., K. Hack, Ed., Woodhead Publishing, 2008, p. 14–42
 20. T. Nishizawa, S.M. Hao, M. Hasebe, and K. Ishida, Thermodynamic Analysis of Miscibility Gap Due to Ordering in Ternary Systems, *Acta Met.*, 1983, **31**(9), p 1403–1416
 21. J.-C. Zhao, Chapter Two-The Role of Phase Transformation Kinetics in Phase Diagram Determination and Assessment, *Methods for Phase Diagram Determination*, Elsevier Science Ltd, Oxford, 2007, p 22–50
 22. A.V. Ruban and V.I. Razumovskiy, First-Principles Based Thermodynamic Model of Phase Equilibria in Bcc Fe-Cr Alloys, *Phys. Rev. B*, 2012, **86**(17), p 1–16
 23. F. Stein, C. He, and N. Dupin, Melting Behaviour and Homogeneity Range of B2 CoAl and Updated Thermodynamic Description of the Al-Co System, *Intermetallics*, 2013, **39**, p 58–68
 24. H. Okamoto, Al-Ni (Aluminum-Nickel), *J. Phase Equilib.*, 1993, **14**(2), p 257–259
 25. C. Davies, P. Nash, R. Stevens, and L. Yap, Precipitation in Ni-Co-Al Alloys, *J. Mater. Sci.*, 1985, **20**(8), p 2945–2957
 26. Y. Tanaka, K. Oikawa, Y. Sutou, T. Omori, R. Kainuma, and K. Ishida, Martensitic Transition and Superelasticity of Co-Ni-Al Ferromagnetic Shape Memory Alloys with $\beta + \gamma$ Two-Phase Structure, *Mater. Sci. Eng. A*, 2006, **438–440**, p 1054–1060
 27. Y.A. Chang, L.M. Pike, C.T. Liu, A.R. Bilbrey, and D.S. Stone, Correlation of the Hardness and Vacancy Concentration in FeAl, *Intermetallics*, 1993, **1**(2), p 107–115
 28. F. Lukáč, J. Čížek, I. Procházka, Y. Jirásková, D. Janičkovič, W. Anwand, and G. Brauer, Vacancy-Induced Hardening in Fe-Al Alloys, *J. Phys. Conf. Ser.*, 2013, **443**, p 12025
 29. B.H. Toby and R.B. Von Dreele, GSAS-II: the Genesis of a Modern Open-source all Purpose Crystallography Software Package, *J. Appl. Crystallogr.*, 2013, **46**(2), p 544–549
 30. K. Shinagawa, T. Omori, J. Sato, K. Oikawa, I. Ohnuma, R. Kainuma, and K. Ishida, Phase Equilibria and Microstructure on γ' Phase in Co-Ni-Al-W System, *Mater. Trans.*, 2008, **49**(6), p 1474–1479
 31. Y. Mishima, S. Ochiai, and T. Suzuki, Lattice Parameters of Ni (γ), Ni₃Al (γ') and Ni₃Ga (γ') Solid Solutions with Additions of Transition and B-Subgroup Elements, *Acta Metall.*, 1985, **33**(6), p 1161–1169
 32. N. Ridley, Defect Structures in Binary and Ternary Alloys Based on CoAl, *J. Inst. Met.*, 1966, **94**, p 255–258
 33. H.J. Kang, S.K. Wu, and L.M. Wu, Martensitic Transformation of Ni₆₄Al₃₄Re₂ Shape Memory Alloy, *Intermetallics*, 2010, **18**(1), p 123–128
 34. T. Nishizawa and K. Ishida, Co-Ni (cobalt-nickel), *Phase Diagrams of Binary Nickel Alloys*, P. Nash, Ed., ASM International, Almere, 1991, p 69–70